arXiv:1702.07512v1 [astro-ph.GA] 24 Feb 2017

ALMA Deep Field in SSA22: Blindly Detected CO Emitters and [CII] Emitter Candidates

N. H. Hayatsu[1*]**, Y. Matsuda**[2, 3]**, H. Umehata**[4, 5]**, N. Yoshida**[1, 6]**, I. Smail**[7]**,
A. M. Swinbank**[7]**, R. Ivison**[8]**, K. Kohno**[5, 9]**, Y. Tamura**[5]**, M. Kubo**[10]**,
D. Iono**[2, 3]**, B. Hatsukade**[2]**, K. Nakanishi**[2, 3]**, R. Kawabe**[2, 3]**, T. Nagao**[11]**,
A. K. Inoue**[12]**, T. T. Takeuchi**[13]**, M. Lee**[2, 14]**, Y. Ao**[2]**, S. Fujimoto**[14, 15]**, T. Izumi**[5]**,
Y. Yamaguchi**[5]**, S. Ikarashi**[16]**, and T. Yamada**[17, 18]

[1] Department of Physics, The University of Tokyo, 7-3-1 Hongo, Bunkyo, Tokyo 113-0033, Japan

[2] National Astronomical Observatory of Japan, Osawa 2-21-1, Mitaka, Tokyo 181-8588, Japan

[3] Graduate University for Advanced Studies (SOKENDAI), Osawa 2-21-1, Mitaka, Tokyo 181-8588, Japan

[4] The Open University of Japan, 2-11 Wakaba, Mihama-ku, Chiba 261-8586, Japan

[5] Institute of Astronomy, School of Science, The University of Tokyo, 2-21-1 Osawa, Mitaka, Tokyo 181-0015, Japan

[6] Kavli Institute for the Physics and Mathematics of the Universe (WPI), Todai Institutes for Advanced Study,
The University of Tokyo, Kashiwa, Chiba 277-8583, Japan

[7] Centre for Extragalactic Astronomy, Department of Physics, Durham University, South Road, Durham, DH1 3LE, UK

[8] European Southern Observatory, Karl-Schwarzschild-Str. 2, D-85748 Garching, Germany

[9] Research Center for the Early Universe, The University of Tokyo, 7-3-1 Hongo, Bunkyo, Tokyo 113-0033

[10] National Astronomical Observatory of Japan TMT Project Office, Osawa 2-21-1, Mitaka, Tokyo 181-8588, Japan

[11] Research Center for Space and Cosmic Evolution, Ehime University, Matsuyama 790-8577, Japan

[12] College of General Education, Osaka Sangyo University, 3-1-1 Nakagaito, Daito, Osaka 574-8530, Japan

[13] Division of Particle and Astrophysical Science, Nagoya University, Furo-cho, Chikusa-ku, Nagoya 464-8602, Japan

[14] Department of Astronomy, Graduate school of Science, The University of Tokyo, 7-3-1 Hongo, Bunkyo-ku, Tokyo 133-0033, Japan

[15] Institute for Cosmic Ray Research, University of Tokyo, 5-1-5 Kashiwa-no-Ha, Kashiwa City, Chiba 277-8582, Japan

[16] Kapteyn Astronomical Institute, University of Groningen, P.O. Box 800, 9700AV Groningen, The Netherlands

[17] Astronomical Institute, Tohoku University, 6-3 Aoba, Aramaki, Aoba-ku, Sendai, Miyagi 980-8578, Japan

[18] Institute of Space and Astronautical Science, JAXA, 3-1-1 Yoshinodai, Sagamihara,

Kanagawa Japan

*E-mail: natsuki.hayatsu@utap.phys.s.u-tokyo.ac.jp

Abstract

We report the identification of four millimeter line emitting galaxies with the Atacama Large Milli/submillimeter Array (ALMA) in SSA22 Field (ADF22). We analyze the ALMA 1.1 mm survey data, with an effective survey area of 5 arcmin^2, a frequency range of 253.1–256.8 and 269.1–272.8 GHz, angular resolution of $0''.7$ and RMS noise of 0.8 mJy beam^{-1} at 36 km s^{-1} velocity resolution. We detect four line emitter candidates with significance levels above 6σ. We identify one of the four sources as a CO(9-8) emitter at $z = 3.1$ in a member of the proto-cluster known in this field. Another line emitter with an optical counterpart is likely a CO(4-3) emitter at $z = 0.7$. The other two sources without any millimeter continuum or optical/near-infrared counterpart are likely to be [CII] emitter candidates at $z = 6.0$ and 6.5. The equivalent widths of the [CII] candidates are consistent with those of confirmed high-redshift [CII] emitters and candidates, and are a factor of 10 times larger than that of the CO(9-8) emitter detected in this search. The [CII] luminosity of the candidates are $4 - 7 \times 10^8$ L$_\odot$. The star formation rates (SFRs) of these sources are estimated to be $10 - 20$ M$_\odot$ yr^{-1} if we adopt an empirical [CII] luminosity - SFR relation. One of them has a relatively low-S/N ratio, but shows features characteristic of emission lines. Assuming that at least one of the two candidates is a [CII] emitter, we derive a lower limit of [CII]-based star formation rate density (SFRD) at $z \sim 6$. The resulting value of $> 10^{-2}$ M$_\odot$yr^{-1}Mpc^{-3} is consistent with the dust-uncorrected UV-based SFRD. Future millimeter/submillimeter surveys can be used to detect a number of high redshift line emitters, with which to study the star formation history in the early Universe.

Key words: Cosmology: Early universe — Galaxies: Formation — Galaxies: Clusters: Individual: SSA22

1 Introduction

The cosmic star-formation history in the early Universe has been studied in optical/near-infrared (NIR) wavelengths, which trace ultraviolet (UV) radiation in rest-frame at high redshifts (e.g., Madau & Dickinson 2014). The UV star formation rate density (SFRD) does not account for all components of star-forming galaxies (e.g., Bouwens et al. 2012; Bouwens et al. 2016). Recent studies suggest that far-infrared (FIR) SFRD contributes more than half of the total at $z = 0 - 4$ (e.g., Blain et al. 1999; Barger et al. 2012; Burgarella et al. 2013; Gruppioni et al. 2013; Swinbank et al. 2014). Millimeter/submillimeter (mm/submm) galaxy surveys would be, in principle, efficient to probe the dust-obscured component of SFRD at high-redshift (Takeuchi et al. 2005; Burgarella et al. 2013; Chen et al. 2016; Carniani et al. 2015; Fujimoto et al. 2016; Aravena et al. 2016a; Dunlop et al. 2017; Umehata et al. 2017). The advantage of such observations in mm/submm is the well-known negative k-correction; the continuum flux of a typical star-forming galaxy of fixed SFR remains approximately constant with increasing redshift (Blain et al. 2002). However, it is often difficult to estimate redshifts for very faint and dusty sources (e.g., Simpson et al. 2014).

Strong emission lines such as [CII]158μm or [OIII] 88μm lines can be used to study the SFR and gas properties of high-z star-forming galaxies as well as to determine their spectroscopic redshifts (e.g., Colbert et al. 1999; Maiolino et al. 2005; Brauher et al. 2008; Swinbank et al. 2012; Venemans et al. 2012; De Looze et al. 2014; Inoue et al. 2014; Willott et al. 2015; Maiolino et al. 2015; Inoue et al. 2016; Carniani et al. 2017). Interestingly, Capak et al. (2015) report that Lyman-break galaxies (LBGs) at $z = 5 - 6$ show enhancement of [CII] emission relative to the FIR continuum compared with mm/submm-selected galaxies. They also serendipitously detected a [CII] emitter which is faint in both the rest-UV and FIR continuum. Combining observations in rest-UV, FIR and mm/submm emission lines appears to be essential to understand the physical properties of galaxies at high redshifts (e.g., Bouwens et al. 2016; Aravena et al. 2016a; Dunlop et al. 2017).

One of the brightest submm emission lines is [CII] (e.g., Maiolino et al. 2005; Maiolino et al. 2009; Iono et al. 2006; Venemans et al. 2012; Swinbank et al. 2012; Willott, Omont, & Bergeron 2013; Willott et al. 2015; Maiolino et al. 2015; Capak et al. 2015; Díaz-Santos et al. 2016; Pentericci

et al. 2016). Carbon in the interstellar medium is largely in a singly ionised state in a variety of environments, from HII regions to molecular clouds, because the ionization potential of atomic carbon is 11.3 eV, lower than that of hydrogen and close to dissociation energy of CO of 11.1 eV (e.g., Wolfire et al. 2010; Carilli & Walter 2013). The critical density of [CII] emission is about 3×10^3 cm^{-3}, and thus [CII] emission can arise even in a molecular cloud with temperature around 92 K (Hollenbach & McKee 1989). Therefore [CII] radiative cooling often dominates in regions with a wide range of densities (e.g., Wolfire et al. 1995; Kaufman et al. 1999). Finally, [CII] emission is thought to be a potential tracer of SFR because of its main origin of photo-dissociated region associated with young, massive stars (e.g., De Looze et al. 2011; De Looze et al. 2014; Sargsyan et al. 2012; Kapala et al. 2015). An important observational advantage is that [CII] line emission at $z > 4$ is redshifted to wavelengths with low atmospheric absorption and thus it is possible to detect [CII] line emission even from galaxies at $z = 7$ (e.g., Venemans et al. 2012; Aravena et al. 2016b; Pentericci et al. 2016).

A number of high-redshift [CII] emitters are expected to be detected with forthcoming high sensitivity observations with the Atacama Large Millimeter/submillimeter Array (ALMA) (e.g., Geach & Papadopoulos 2012; da Cunha et al. 2013; Matsuda et al. 2015; Aravena et al. 2016b). In this paper, we present a blind search for [CII] emitters using ALMA Cycle 2 data (Umehata et al. 2017). We briefly introduce the observations in §2. The details of our data analysis is described in §3. Then we show the results in §4 and discuss the implications for cosmic star formation history in §5. We summarize the results and discussions in §6. Throughout the paper, we adopt the standard ΛCDM cosmology with the matter density $\Omega_{\rm M} = 0.3$, the cosmological constant $\Omega_\Lambda = 0.7$, the Hubble constant $h = 0.7$ in the unit of $H_0 = 100$ km s^{-1}Mpc^{-1}. All magnitudes are given in the AB system, unless otherwise noted. We calculate SFR assuming Chabrier initial mass function (IMF) (Chabrier 2003), with an integration range from 0.08 M$_\odot$ to 100 M$_\odot$. When needed, we use the conversion factor of 1.8 from the Chabrier IMF to the equivalent Salpeter IMF (Salpeter 1955) and 1.1 from the Chabrier IMF to the Kroupa IMF (Kroupa 2001).

2 Observation

We analyze data from the ALMA Deep Field survey of SSA22 (ADF22) observed in Band 6 in ALMA Cycle 2 in June 2014 and April 2015 (Proposal ID 2013.1.00162.S, PI: H. Umehata). The details of the observation are described in Umehata et al. (2017).

ADF22 is a survey field with an area of $2' \times 3'$ centered on a $z = 3.09$ proto-cluster; RA (J2000) = $22^{\rm h}17^{\rm m}34^{\rm s}$, Dec (J2000) = $+00°17'00''$ consisting of 103 pointing fields. The field was

observed using four 1.875 GHz spectral windows (SPW) with the central frequency of 263 GHz, which corresponds to the [CII] redshift of $z = 6.2$.

The typical angular resolution of a combined data is $0''.72 \times 0''.62$ corresponding to ~ 6 kpc at $z = 6.2$. The on-source time per pointing in the fields is 4.5 min. The data observed in 2014 and 2015 have angular resolution of $0''.54 \times 0''.49$ and $1''.24 \times 0''.87$, and on-source time per pointing in the fields of 2.5 min. and 2.0 min. for 2014 and 2015, respectively.

The four SPWs have root-mean-square (RMS) noise level of 0.7, 0.7, 0.8 or 0.9 mJy beam^{-1} at a 36 km s^{-1} velocity resolution. The RMS of each SPW at 36 km s^{-1} resolution of combined, 2014 and 2015 data as a function of the observed frequency are shown in Figure 1, where no significant atmosphere absorption is seen. Other properties of the data are listed in Table 1.

In order to search faint emission line sources, we use high sensitivity data of 80 pointing fields; Field 1 - Field 80 and search in a rectangle area of ~ 5 arcmin^2; (RA (J2000), Dec (J2000)) = ($22^{\rm h}17^{\rm m}31.86^{\rm s}$, $+00°15'25.46''$) to ($22^{\rm h}17^{\rm m}38.17^{\rm s}$, $+00°18'35.05''$), and a frequency coverage of 253.1–272.8 GHz (Table 1). The effective survey area corresponds to about 29 comoving Mpc^2 and the effective survey volume is $\sim 2.2 \times 10^3$ comoving Mpc^3 at $z = 6.2$.

3 Method

The flowchart of our source selection method is shown in Figure 2. The data are analyzed with Common Astronomy Software Application (CASA) ver. 4.5.3 (McMullin et al. 2007). We make continuum-subtracted datacube by using UVCONTSUB and CLEAN. We first spectrally smooth the data to obtain high signal-to-noise (S/N) ratios. The top-hat spectral smoothing window is set to be 0, 2, 4, ..., 12, 15, 18, ..., 21 slices, with a slice width corresponding to ~ 18 km s^{-1}. We use the spectral smoothing function "boxcar" so that the velocity sampling of the output data is kept constant. As each spectral data slice has a different RMS value as shown in Figure 1, we normalise each slice by its RMS. We call a datacube thus-generated as "S/N cube".

We use CLUMPFIND (Williams, de Geus, & Blitz 1994) to search emission line sources in the S/N cube. We search for sources with a threshold value "low" of CLUMPFIND of ≥ 4.5. We then do 'matching' of the clumps detected at the same position between the S/N cubes in the same SPW with different resolutions and retain the clump that has maximum S/N ratio (see also Table 1). We select clumps that have the S/N ratio larger than 6.0σ and also larger than the maximum negative S/N ratio measured in the inverted S/N cube in each SPW (see also Figure 2), in order to avoid contamination by spurious sources (e.g., Hatsukade et al. 2016). We also check line spectral fea-
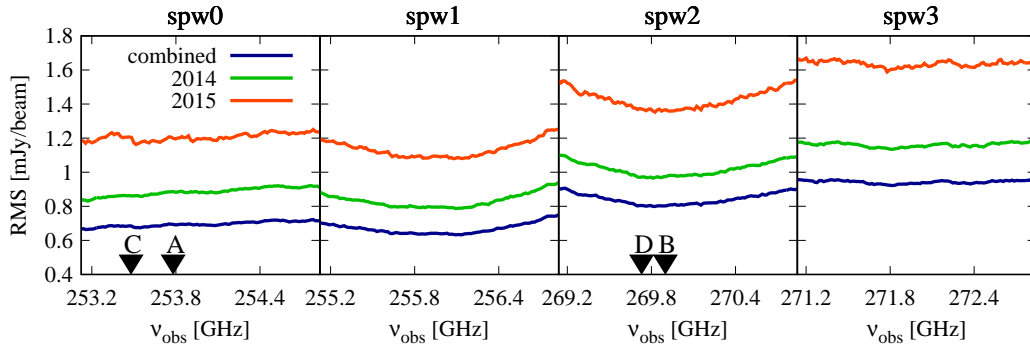
Fig. 1. The RMS noise level of the four spectral windows (SPWs) analyzed in this work at 36 km s^{-1} velocity resolution as a function of observed frequency. In each panel, we plot the RMS of combined data and the individual data obtained in 2014, and in 2015, respectively. We also mark the frequencies of the detected four line emitter candidates A–D. Typical RMS values are also given in Table 1. We note that the data observed in 2014 and 2015 have different angular resolutions.

tures of the detected clumps (sources) in the datacube separately for those observed in 2014 and 2015.

For the detected sources, we search for their counterparts in u^* band taken with the Canada France Hawaii Telescope/MegaCam obtained by archival data (Kousai 2011), B, V, R, i', z', NB912, J, H, K band taken with the Subaru Telescope (Hayashino et al. 2004; Nakamura et al. 2011; Suzuki et al. 2008; Uchimoto et al. 2012), 3.6 μm, 4.5 μm, 5.8 μm, 8.0 μm, 24 μm taken with the *Spitzer* Space Telescope/IRAC and MIPS (Hainline et al. 2009; Webb et al. 2009) 0.5 keV, 2 keV and 8 keV taken with the *Chandra* X-Ray Observatory (Lehmer et al. 2009).

[CII] line emitting galaxies at $z = 6.0 - 6.5$ are likely to be detected only longward of z' band and/or in narrowband NB912 if they are LBGs or Lyα emitters (LAEs) (e.g., Nakamura et al. 2011), although the available z' band and NB912 data could be too shallow for high-redshift [CII] emitters in our blind search. For the sources with counterparts, we estimate either their photometric redshift by means of spectral energy distribution (SED) fitting or spectroscopic redshift by assuming their line species. SED fitting is calculated by using HYPERZ software (Bolzonella et al. 2000). In §4.3, we also use the equivalent width and the source number density to consider if the detected [CII] emitter candidates are other line emitters.

4 Result

4.1 Source Detection

We detect four line emitter candidates. Hereafter, we call the two sources without optical, NIR and FIR counterparts ADF22-LineA and ADF22-LineB. Those with counterparts are dubbed as ADF-LineC and ADF-LineD. The peak S/N ratio are 6.5σ, 6.2σ, 7.7σ and 6.5σ, for ADF22-LineA, B, C and D, respec-
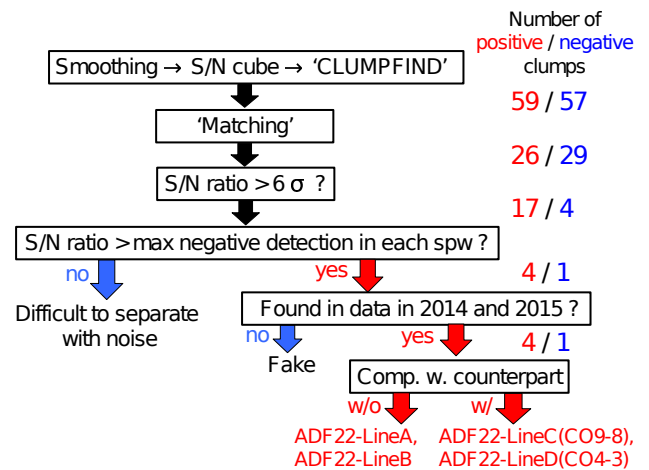

Fig. 2. Flowchart of the our selection method. The number of the retained clumps with $> 5.5\sigma$ at each step is given on the right. We select the targets by setting a S/N threshold 6.0σ in each SPW, and then by imposing that their S/N are larger than the maximum negative S/N ratio (see also Table 1). Finally, the selection leaves four clumps as line emitting galaxy candidates.

tively. The first moment images of the candidates are shown in Figure A, and their properties are shown in Table 2.

Figure 3 shows the cumulative number of positive and negative clumps as a function of S/N ratio. Although the S/N ratios of ADF22-LineA, B and D are below 6σ at the original spectral sampling, the lines are detected at $\geq 6\sigma$ in the smoothed S/N cubes. We compare the spectral line features of the emitter candidates in different observation epochs, 2014 and 2015 (Figure 4). Overall, the contiguous positive signals over a velocity range of ≥ 180 km s^{-1} and the line features commonly seen suggest that the candidates are likely real sources.

We note here that we also detect one clump with 6.3σ in the inverted S/N cube, and thus we would naively be concerned that
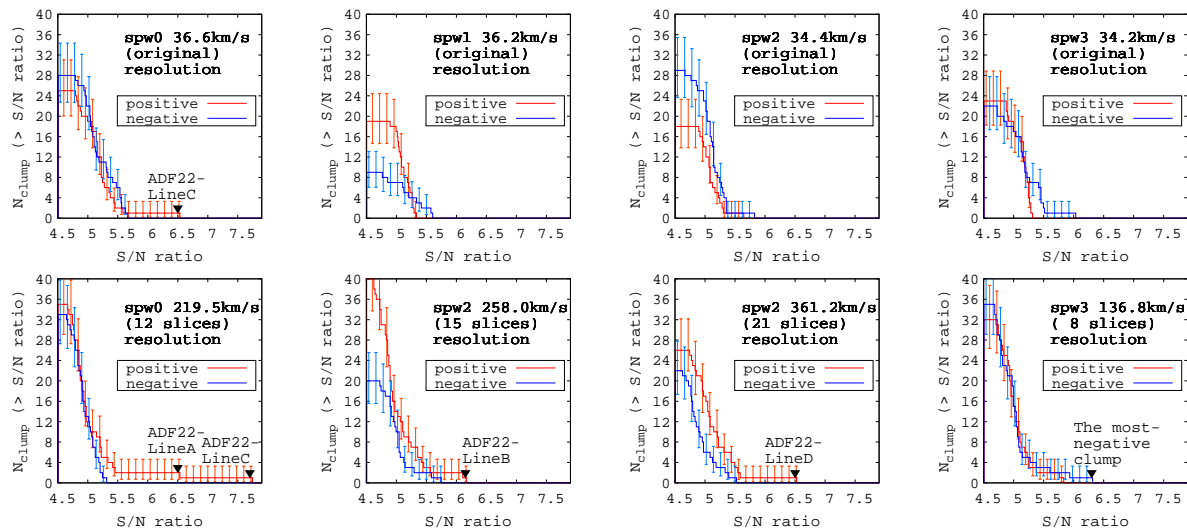
Fig. 3. Cumulative number of the positive and negative clumps as a function of S/N, with 1σ error bar from the source number statistics (Gehrels 1986). We use the continuum-subtracted S/N cubes before 'matching'. Top panels show the number distributions with our fiducial spectral resolution. ADF22-LineC is detected with 6.5σ in S/N cube at the fiducial resolution. Bottom panels show the result with smoothed spectral resolutions. ADF22-LineA and ADF22-LineC are detected in the S/N cube at 220 km s^{-1} spectral smoothing, ADF22-LineB at 258 km s^{-1} spectral smoothing, and ADF22-LineD at 361 km s^{-1} spectral smoothing. ADF22-LineD is also detected with 6.1σ at 258 km s^{-1} spectral smoothing. The most-negative clump detected in SPW 3 has a S/N ratio of 6.3σ in the inverted S/N cube.

one candidate with 6.2σ could be a spurious source. However, the most-negative clump is actually detected in SPW 3, where none of our four candidates is located. We also find that datacubes with higher RMS value have higher maximum negative detection (Table 1). Since the datacubes in different SPWs have different properties, the existence of the high-σ negative clump in SPW 3 does not immediately impacts the confidence of our line emitter candidates. ADF22-LineB has a lower S/N ratio than ADF22-LineA, whereas it has non-negative z' band counterparts with $< 3\sigma$ (see also Figure 5). Velocity-gradient is also seen around ADF22-LineB (see also Figure A).

4.2 Line Identification

Figure 5 shows the images of the four candidates in B, V, z', 3.6 μm and 1.1 mm wavebands. We plot SED and model fit for ADF22-LineD in Figure B, and the measured photometry in the detected bands are given in Table 3. The photometric redshift is estimated by using HYPERZ (Bolzonella et al. 2000). We fit the SED templates by Bruzual & Charlot (1993) to the spectral coverage from UV to 8 μm, assuming a Calzetti dust extinction law (Calzetti et al. 2000). We also use SED templates from SWIRE library (Polletta et al. 2007).

ADF22-LineA and B: We do not find any secure counterpart nor close sources within $2''$ of the sources. Therefore we regard LineA and LineB as good [CII] emitter candidates.

ADF22-LineC: LineC very likely arises from the galaxy ADF22.4 reported in Umehata et al. (2017), whose redshift is determined to be $z = 3.091$ from far-infrared spectroscopic fol-

low up observations (Umehata et al. in prep.). Thus we identify ADF22-LineC as CO(9-8) line emission at $z = 3.091$. In addition, the optical component near ADF22-LineC is a known galaxy at $z = 0.55$ (Kubo et al. 2015), but we exclude possibility of ADF22-LineC to be at $z = 0.55$ because there is no obvious line species observed at 1.1 mm. LineC is also detected in X-ray (Lehmer et al. 2009), which may indicate that ADF22-LineC is an AGN-host galaxy. Further details of the galaxy will be discussed in Umehata et al. (in prep.).

ADF22-LineD: LineD is spatially consistent with the position of a tentatively detected continuum source ADF22.21 reported in Umehata et al. (2017). The result of SED fitting shows that reduced χ^2 values becomes minimum at $z \sim 0.6 - 0.8$ (Figure B left). Interestingly, the SED is well fitted by that of Arp220 placed at $z \sim 0.7$ (Figure B right). By searching for possible lines in this redshift range, we conclude that ADF22-LineD is likely a CO(4-3) emitter at $z = 0.71$.

4.3 Possibility of other line emissions

Besides the [CII] line emission, there are also possibilities that ADF22-LineA and LineB are other emission line sources, such as ^{12}CO line emission at $z \leq 3.1$, H$_2$O at $z \sim 1.9$ or 2.8, [NII]205μm at $z \sim 4.6$, [OI]145μm at $z \sim 6.9$, [NII]122μm at $z \sim 8.5$ or [OIII]88μm at $z \sim 12$ (Swinbank et al. 2012; Tamura et al. 2014; Ono et al. 2014; Decarli et al. 2016a; Aravena et al. 2016b).

If ADF22-LineA and LineB are ^{12}CO emitters, the number density is consistent with the result of ASPECS survey
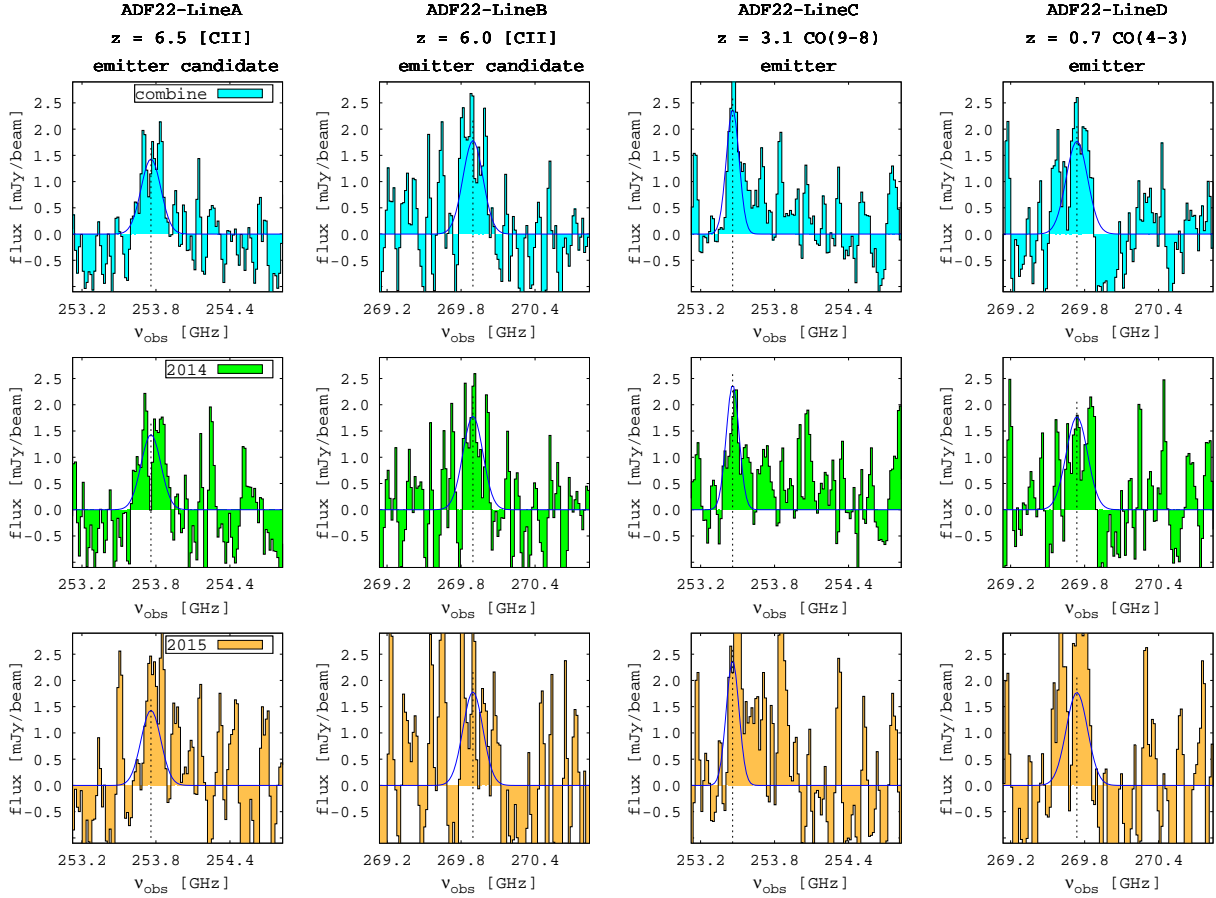
Fig. 4. The spectra of our four line emitter candidates . We use continuum-subtracted image data in original spectral resolution. Top panels show the combined data observed in 2014 and 2015, whereas the middle and the bottom panels show separately the data observed in 2014 (green) and the data observed in 2015 (orange). The blue curve in each panel shows the best fit Gaussian profile for the combined data. ADF22-LineA and LineB are the candidate [CII] emitters from our survey.

(Decarli et al. 2016a) and with semi-analytical/empirical predictions referred to the article (Lagos et al. 2012; Popping et al. 2016; Vallini et al. 2016). Thus we cannot exclude the possibility of ^{12}CO emitters by the discussion of detectability.

We compare the equivalent widths (EWs) in observed frame of the four candidates. The estimated EWs are > 8.6, > 14.6, 1.1 and 7.3 μm for ADF22-LineA, B, C and D, respectively, assuming 3σ continuum flux limit. ADF22-LineA and B have higher EW than the blindly detected ^{12}CO emitters in our survey. The left and middle panels of Figure 6 also show the distribution of the EWs in 0.9–1.3 mm observed frame of the four candidates, high-redshift [CII] emitting LBGs and LAEs (Capak et al. 2015; Pentericci et al. 2016), [CII] emitter candidates detected in ASPECS (Aravena et al. 2016b), ^{12}CO emitter candidates detected in band 6 in ASPECS (Decarli et al. 2016b). The EWs of ADF22-LineA, B and other high-redshift [CII] emitter/candidates are comparable. Given these information, we argue that ADF22-LineA and B are more likely [CII] emitters at $z = 6.5$ and 6.0, rather than CO emitters at $z \leq 3.1$. EW values of ADF22-LineA and B are comparable to those of the

blindly detected CO emitters. Further consideration by using forthcoming follow up observation and theoretical study will be needed to yield any insight about the trends of EW distributions. As with ADF22-LineA and B, blindly detected line emitter candidates are expected to have often no counterpart (Aravena et al. 2016b). Thus it is important to study the EWs of a large sample of CO/[CII] emitters. We note that H_2O molecular lines are expected to have similar line flux to CO line emission in the submm band (e.g, Rangwala et al. 2011; Omont et al. 2013), and thus can be distinguished from high-redshift [CII] emitters by comparing their EWs.

[CII] luminosity, $L_{[CII]}$ of ADF22-LineA and B is calculated by using luminosity distance D_L, observed frequency ν_o, velocity-integrated flux S^v (e.g., Carilli & Walter 2013),

$$\frac{L_{[CII]}}{L_\odot} = 1.04 \times 10^{-3} \left(\frac{D_L}{\mathrm{Mpc}} \right)^2 \frac{\nu_o}{\mathrm{GHz}} \frac{S^v}{\mathrm{Jy\ km\ s^{-1}}}. \quad (1)$$

The estimated $L_{[CII]}$ of $4 - 7 \times 10^8$ $L_\odot$ is consistent with the values of normal star-forming galaxies in the local universe (e.g., Swinbank et al. 2012), thus we do not consider the effect
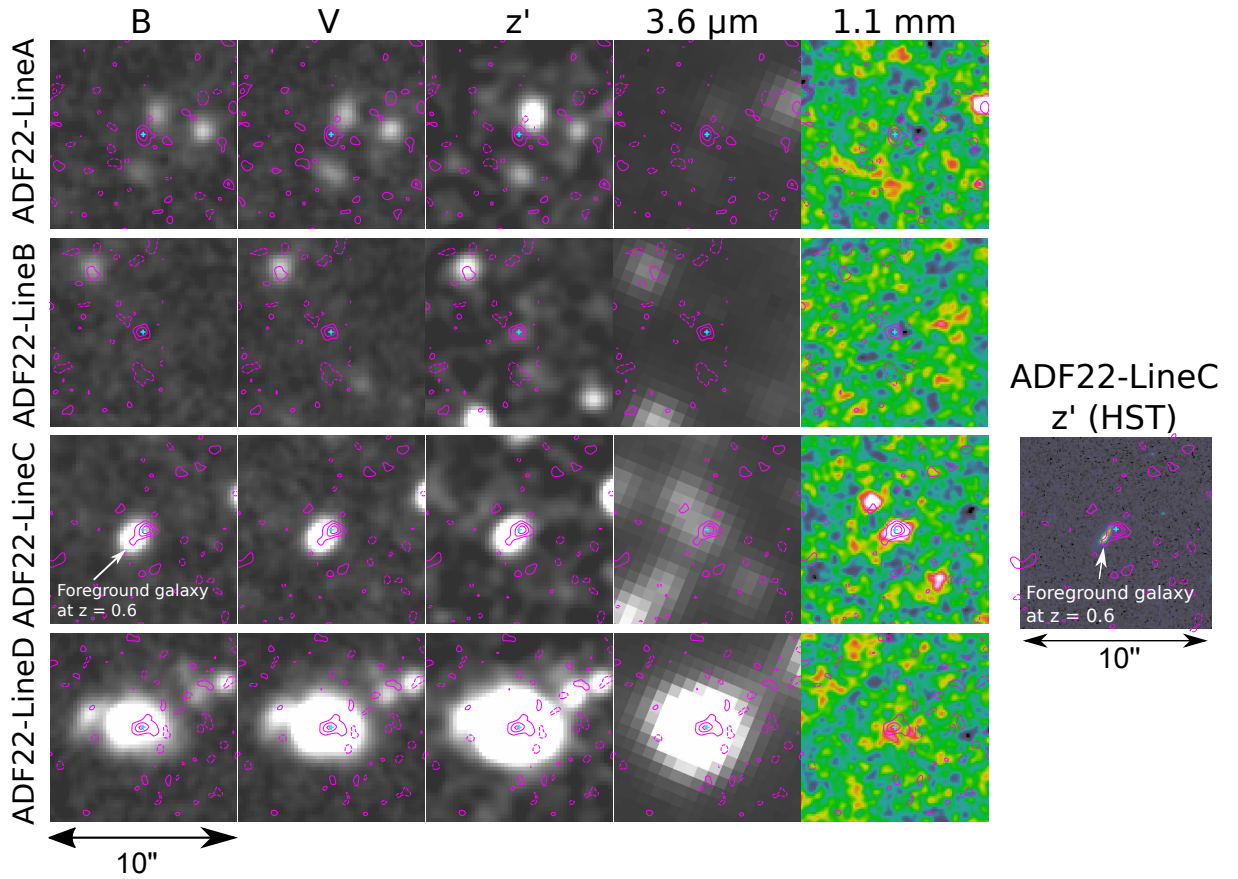
Fig. 5. Images of the four line-emitter candidates at different wavelength range from optical to 1.1 mm. In each panel, the cyan cross indicates the position of the candidate. The magenta contours show the 0th moment images of the line emission with 2, 4, and 6σ, and the dashed contours with -4 and -2 σ. We adopt a linear colour-scale for this figure. Counterparts are not found at the position of LineA and LineB at any wavelength. We also show a z' band image of LineC taken by *HST* Advanced Camera for Surveys I (F814W)-band in archive (PID 9760) in the rightmost panel.
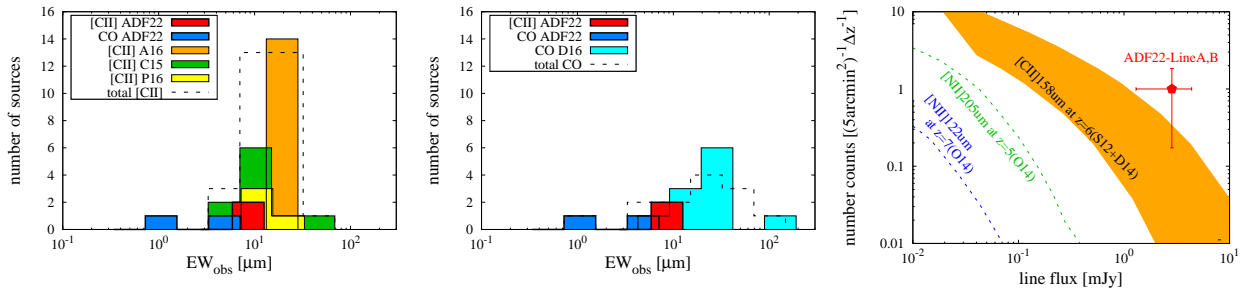
Fig. 6. *Left and middle*: We compare the distribution of EWs in 0.9–1.3 mm observed frame: The ADF22 sources with high redshift [CII] emitters/candidates (left) and low-redshift CO emitters/candidates (middle) (Capak et al. 2015; Aravena et al. 2016b; Pentericci et al. 2016; Decarli et al. 2016b). Continuum upper limit is assumed to be 3σ. The histograms except for the case of ADF22 CO emitters contain the data with lower limits. EW values of ADF22 [CII] emitter candidates are comparable to other high-redshift [CII] emitters/candidates and ADF22 CO emitters have in relatively lower values. For CO emitters, their transition are $j = 9$–8 to 3–2, which are not corrected to fixed transition. ADF22 [CII] emitter candidates are consistent with the CO distribution using observational data available. *Right*: The cumulative number counts of [NII]-, and [CII]-line emitters, where Δz is set to be the survey redshift range. Red point represents number density of this survey for one [CII] emitter candidate with 1σ error bar from the source number statistics (Gehrels 1986). Orange shaded region shows the [CII] emitter number count estimated (converted) from the star formation rate function at $z = 6$ (Smit et al. 2012) and SFR-$L_{\rm [CII]}$ relation (De Looze et al. 2014). The velocity width is assumed to be 200 km s^{-1}. This simple model shows agreement to the observed number count. The dotted lines show [NII]-emitter number counts from Orsi et al. (2014), which are well below the observational result. We also note the [OIII] number counts at $z \sim 12$ are below of the [NII]122μm counts (Orsi et al. 2014).
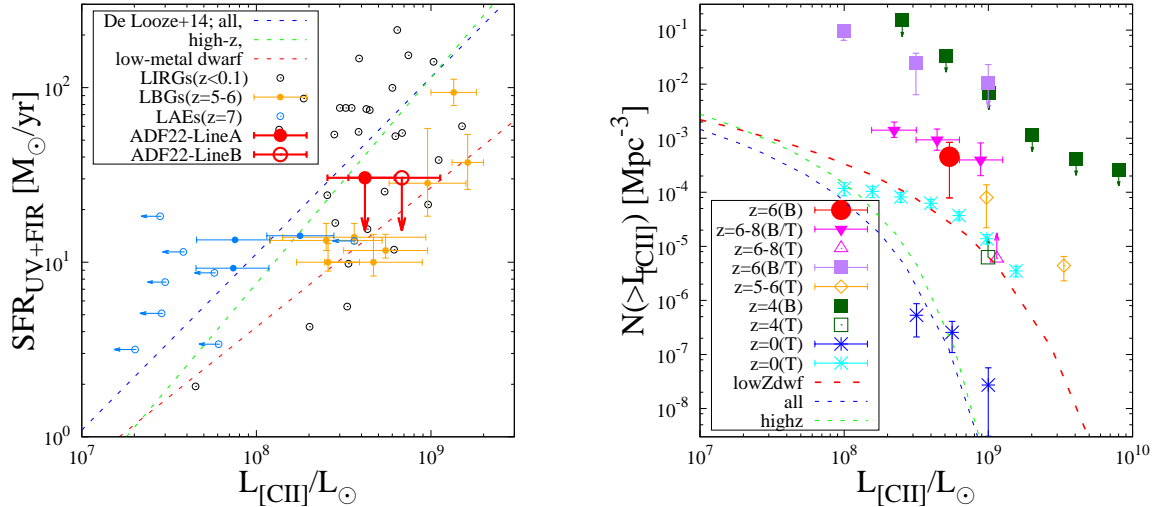
Fig. 7. *Left*: We compare the [CII] emitter candidates with other local luminous infrared galaxies (LIRGs) (Maiolino et al. 2009), LBGs at $z = 5.2 - 5.7$ (Capak et al. 2015), and LAEs at $z = 6.6 - 7.2$ (Pentericci et al. 2016) in the SFR - $L_{[CII]}$ plane. The dashed lines represent empirical SFR-$L_{[CII]}$ relations by De Looze et al. (2014) for different populations. The SFR-$L_{[CII]}$ relation for metal poor dwarfs is consistent with the upper limit of SFR$_{UV+FIR}$ of [CII] emitter candidates. *Right*: We summarize the redshift evolution of the [CII] luminosity function ([CII] LF) (Swinbank et al. 2012; Hemmati et al. 2017; Matsuda et al. 2015; Capak et al. 2015; Miller et al. 2016; Aravena et al. 2016b). The estimations from targeted observations are denoted by (T), and blind surveys are denoted by (B). We estimate [CII] LF at $z = 6.2$ from blind detection on the assumption that one of the two unconfirmed lines is [CII] line at $z \sim 6$. The error-bar on our point uses Gehrels (1986). We also plot model of [CII] LFs at $z = 6$ calibrated by using the star formation rate function at $z = 6$ (Smit et al. 2012) and the SFR-$L_{[CII]}$ relation by De Looze et al. (2014). The observational results at $z > 4$ show good agreement with the predicted LF for metal poor dwarfs.

of [CII] line deficit (e.g., Graciá-Carpio et al. 2011; Díaz-Santos et al. 2013). We then derive [CII] luminosity function by using SFR-[CII] luminosity relation (De Looze et al. 2014) and SFR function at $z = 6$ (Smit et al. 2012). The right panel of Figure 6 shows that the detection of one [CII] emitter candidate in the survey area is roughly consistent with the expected [CII] number counts, if we use the SFR-$L_{[CII]}$ relation by De Looze et al. (2014) that is calibrated from observations of nearby low-metallicity dwarf galaxies (see also §5):

$$\frac{\text{SFR}_{[CII]}}{\text{M}_\odot \text{yr}^{-1}} = 10^{-5.73 \pm 0.32} \left(\frac{L_{[CII]}}{\text{L}_\odot} \right)^{0.80 \pm 0.05}. \quad (2)$$

We also plot the predicted number counts of [NII] 122μm and [NII] 205μm from the model of Orsi et al. (2014). The predicted number count of [OIII] 88μm emission at $z \sim 12$ are lower than the [NII] 122μm emission (Orsi et al. 2014). It is expected that such line emitters will not be found in our survey area. From the discussion above, we assume ADF22-LineA and B to be [CII] emitter candidates.

5 Discussion

In order to discuss the cosmic star formation history, we derive the SFRs of ADF22-LineA and ADF22-LineB assuming that they are [CII] emitters at $z = 6$. We calculate total SFR by summing up the dust-uncorrected SFR$_{UV}$ and SFR$_{IR}$,

SFR$_{UV+IR}$(e.g., Buat et al. 2010), by using the following equations (Kennicutt 1998);

$$\frac{\text{SFR}_{UV}}{\text{M}_\odot \text{ yr}^{-1}} = 7.8 \times 10^{-29} \frac{L_\nu}{\text{ergs s}^{-1} \text{ Hz}^{-1}}, \quad (3)$$

$$\frac{\text{SFR}_{IR}}{\text{M}_\odot \text{ yr}^{-1}} = 2.5 \times 10^{-44} \frac{L_{IR}}{\text{ergs s}^{-1}}, \quad (4)$$

where L_ν refers to the UV luminosity density in the wavelength range 1500-2800 Å, and L_{IR} refers to the IR luminosity integrated over 8-1000 μm. We estimate L_{IR} of ADF22-LineA, B and D from the observed 1.1 mm continuum fluxes by using the SED fitting method of Chary & Elbaz (2001). Continuum upper limits of LineA and B are assumed to be 3σ. L_{IR} of ADF22-LineC is referred to estimation of Umehata et al. (2017). Upper limit of UV luminosity is estimated in Nakamura et al. (2011). The obtained SFR$_{UV+FIR}$ is < 30 M$_\odot$yr^{-1}, being consistent with the SFR-$L_{[CII]}$ relation of De Looze et al. (2014) that is calibrated by local low-metallicity dwarf galaxies (Figure 6 left). We note that the relation calibrated by high-z galaxies is considered to be applicable to bright [CII] emitters with $> 10^9$L$_\odot$ (De Looze et al. 2014) and exceeds the SFR$_{UV+FIR}$ upper limit for the candidates in this survey. The estimated SFR$_{[CII]}$ from the low-metal dwarf relation are 13^{+4}_{-5} and 20^{+9}_{-10} M$_\odot$/yr for ADF22-LineA and LineB, respectively (see also Table 3).

We estimate the [CII] luminosity function (LF) at $z \sim 6.2$ from only one source, because one of the two [CII] candidates
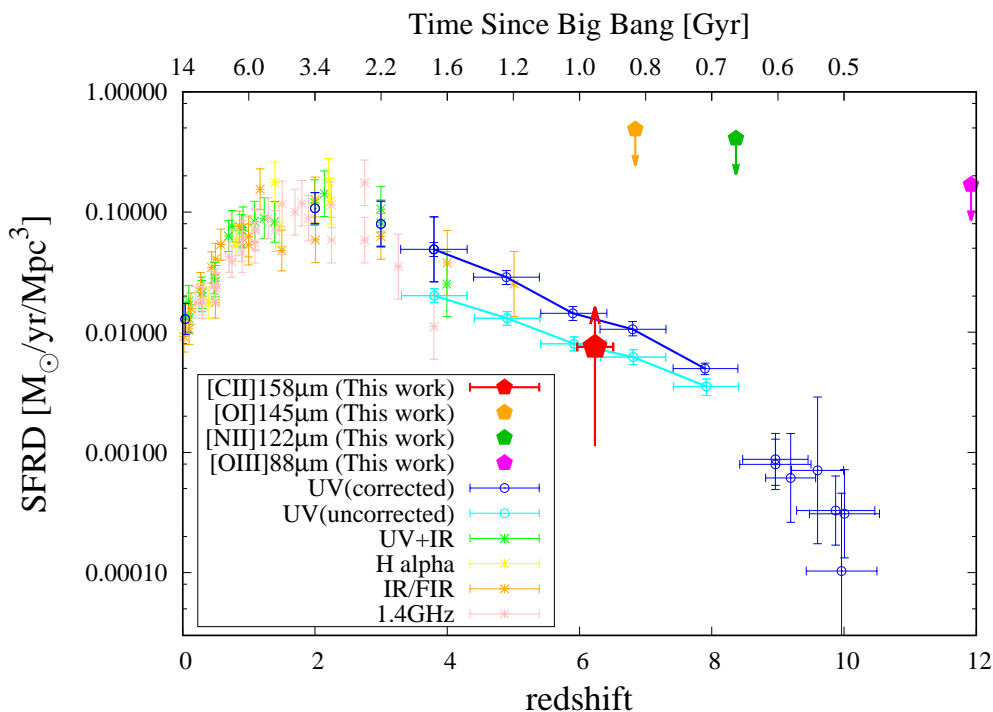
Fig. 8. The cosmic star-formation rate density (SFRD) as a function of redshift. We show lower limit of a [CII] SFRD at $z = 6$ derived from the mean SFR of the two [CII] candidates divided by the survey volume. We also estimate the upper limits for the un-detected fine-structure lines at $z = 7 - -12$. We plot the SFRD estimated by rest-frame UV observations (Oesch et al. 2014; Capak et al. 2015) and other wave bands (Behroozi et al. 2013). The estimation of [CII] SFRD from a conservatively selected one source is already consistent with the dust-uncorrected UV SFRD at $z = 6$.

has a relatively low-σ and thus could possibly be a spurious source (see §4.1). We show this result in Figure 7 and compare it to [CII] LFs from previous studies. The estimated [CII] LFs at $z = 0.0$ (Swinbank et al. 2012; Hemmati et al. 2017) are derived from the follow up observation of the *IRAS* sources (Brauher et al. 2008) or samples from the Great Observatories All-sky LIRG Survey (Díaz-Santos et al. 2013). We indicate the upper limit at $z = 4.4$ derived by Matsuda et al. (2015) using ALMA Cycle 0 archive data, and the lower limit at $z = 4.4$ based on two serendipitous detection in ALESS survey (Swinbank et al. 2012). The estimation at $z = 5 - 6$ is derived from follow up observation by Capak et al. (2015). We also indicate the estimation of over-dense region at $z = 6$ by Miller et al. (2016) . The constraint for [CII] LF at $z = 6 - 8$ is provided by result of ASPECS (Aravena et al. 2016b), which is based on an assumption that all [CII] candidates are real [CII] emitters. As discussed In §4.2, We also derive the simple model of [CII] luminosity function at $z = 6$ by using SFR-$L_{[CII]}$ relation (De Looze et al. 2014) and SFR function at $z = 6$ (Smit et al. 2012). Our [CII] LF model is close to our own observational result and the other studies, whereas the estimated LFs based on the empirical relations for high-redshift, and for all galaxies (De Looze et al. 2014), do not match the observational result at $z > 4$. We note that if completeness of the detection is lower than unity, the estimated

[CII] LF represents the lower limit.

We calculate a conservative limit of [CII] SFRD from the mean of the $\mathrm{SFR}_{[CII]}$ of the two sources divided by the survey volume (Figure 8). The derived [CII] SFRD is $> 7.5 \times 10^{-3} \mathrm{M}_\odot \mathrm{yr}^{-1} \mathrm{Mpc}^{-3}$. Interestingly, this is close to the dust-uncorrected UV SFRD at $z = 6.2$. The contribution of the only one [CII] emitter with faint UV and dust emission to the cosmic SFRD might already constitute a major contribution. The result may imply the existence of the untraceable component of the SFRD by rest-UV. In order to confirm the truth of this, the estimation of a faint end slope of the [CII] LF would be crucial.

In figure 8, we also derive upper limits of SFRDs at $z = 7 - 12$ from the non-detections of [OI] 145μm, [NII] 122μm [OIII] 88μm lines in our search as discussed in §4.3. The SFRs are calculated from line luminosities by using observational relations estimated by Farrah et al. (2013). This result demonstrates that line survey enables us to estimate SFRDs at multiple redshifts at once.

There are a few possible mechanisms for the [CII] line emission to be particularly intense relative to FIR and UV emission. For example, it can be caused by high far-UV radiation from massive, young stars in the early universe (e.g., Wolfire et al. 1995). The environment of a low metallicity and a low dust-to-gas ratio can also cause enhancement of [CII] radiative

cooling (Wolfire et al. 1995; Capak et al. 2015). In particular, the low dust-to-metal environment may not only enhance [CII] line emission but also weaken dust continuum emission (Inoue 2003; Asano et al. 2014). Hot dust dominates the short-wavelength portion of the SED (Casey et al. 2014; Zhou et al. 2016), making the dust continuum at long-wavelengths to be relatively suppressed. The size distribution of dust grains also affect faint FIR continuum (Takeuchi et al. 2003; Takeuchi et al. 2005). Altogether, observations in the submm-band can provide invaluable information on the physical properties of high-redshift galaxies. Future deep submm surveys will enable us to understand the formation of galaxies and to probe the early cosmic star-formation history.

Summary

We search millimeter line emitters by using 1.1 mm ADF22 survey data taken in ALMA Cycle2. Our newly constructed method for line search worked for detecting two CO emitters at $z = 0.7$ and 3.1 and two [CII] emitter candidates at $z = 6.0$ and 6.5 with $> 6\sigma$. [CII] emitter candidates are faint in all counterparts. The line species of the CO emitters are identified by SED fitting or spectral follow up observation. For [CII] emitter candidates, the possibility of other line emissions are excluded by discussion about number counts, line ratio and EWs. Since one spurious source is possibly contaminated with the candidates, we assume at least one of the two candidates to be a real [CII] emitter. We constrain $z = 6$ [CII] LF for one source and found that the [CII] LFs at $z > 4$ show good agreement with the predicted LF by using SFR-$L_{\rm[CII]}$ relation calibrated by local metal poor dwarfs. We also found that estimated [CII]-based SFR are consistent with upper limit of total SFR if we use the SFR-$L_{\rm[CII]}$ relation for local metal poor dwarfs. We estimate a conservative limit of [CII] SFRD at $z = 6.2$ for one source, which is close to the dust-uncorrected UV SFRD at $z = 6.2$. The results might be imply that mm/submm line survey is a powerful probe to estimate untraceable SFRD component from rest-UV observation at high-redshift. The constrain for faint end slope of [CII] LF from further line survey and FIR/UV follow-up observation will give us the truth of such implication and detailed picture of cosmic star-formation history.

Table 1. PROPERTIES OF DATACUBE OF FOUR SPECTRAL WINDOWS.

SPW ID	$\nu_{\rm obs}$[1] [GHz]	$z_{\rm [CII]}$[2]	dv[3] [km s^{-1}]	angular resolution[4] [arcmin]	RMS of original data[5] [mJy/beam]	# of net clumps[6]	# of matched clumps	max positive S/N ratio	max negative S/N ratio
0	253.12 – 254.83	6.458 – 6.508	18.3	0.67, 0.53, 1.09	0.7, 0.9, 1.2,	25 /18	9 /10	7.77σ (10)[7]	5.70σ (2)
1	255.14 – 256.83	6.400 – 6.449	18.1	0.68, 0.54, 1.11	0.7, 0.8, 1.1,	6 /4	5 /3	5.73σ (6)	5.81σ (0)
2	269.14 – 270.84	6.017 – 6.062	17.2	0.62, 0.49, 1.02	0.8, 1.0, 1.4,	18/14	7 /6	6.51σ (21)	6.05σ (6)
3	271.14 – 272.84	5.966 – 6.009	17.1	0.62, 0.49, 1.01	0.9, 1.2, 1.6,	10/21	5 /10	5.99σ (21)	6.30σ (8)

[1] Observed frequency range we use for the search.

[2] [CII] redshift range corresponding to the observed frequency range.

[3] Mean velocity corresponding to an interval of slices.

[4] Mean angular resolution. Column shows combined data, 2014 data and 2015 data, respectively.

[5] 1 σ sensitivity at 36 km s^{-1} spectral resolution calculated by using primary beam corrected data. Column shows in the same manner to (4).

[6] Number of clumps detected by CLUMPFIND (Williams, de Geus, & Blitz 1994) in original/inverted S/N cubes.

[7] Numbers in bracket represent the size of slices smoothed in spectral domain of the S/N cube.

Table 2. MEASURED AND DERIVED CANDIDATE PROPERTIES.

ADF22 ID	Name (J2000)	$\nu_{\rm peak}$ [GHz]	S$_{\rm peak}$/N[1] [σ]	Smoothing[2] [km s^{-1}]	$S_{\rm 1.1mm}$[3] [mJy]	$S_{\rm line}$[4] [Jy km s^{-1}]	FWHM[5] [km s^{-1}]	EW$_{\rm obs}$ [μm]	z[6]	$\log_{10}L_{\rm line}$[7] [$L_\odot$]	$\log_{10}L_{\rm FIR}$[8] [$L_\odot$]
ADF22-LineA	ALMAJ221737.43+001710.7	253.79	6.5	220 (12)	< 0.2	0.4±0.1	220±40	> 8.6	6.489	$8.6^{+0.2}_{-0.2}$	< 11.4
ADF22-LineB	ALMAJ221731.95+001820.3	269.92	6.2	258 (15)	< 0.2	0.7±0.1	220±45	> 14.6	6.041	$8.8^{+0.2}_{-0.3}$	< 11.4
ADF22-LineC	ALMAJ221736.97+001820.8	253.49	7.8	220 (12)	2.0±0.1	0.5±0.1	140±20	$1.1^{0.2}_{-0.2}$	3.091	$8.0^{+0.2}_{-0.2}$	$12.6^{+0.2}_{-0.1}$
ADF22-LineD	ALMAJ221733.07+001718.8	269.70	6.5	361 (21)	0.7±0.2	1.0±0.1	240±40	7.3^{+5}_{-2}	0.709	$6.7^{+0.2}_{-0.3}$	$11.9^{+0.2}_{-0.2}$

(1) The maximum S/N ratio of the clump in all S/N cubes.

(2) The smoothing window of the datacube with maximum positive S/N ratio. Numbers in bracket represent the corresponding size of slices.

(3) 3σ upper limit is estimated in Umehata et al. (2017).

(4) The integrated line flux estimated by IMFIT.

(5) Full width half maximum derived by gaussian fit.

(6) The redshift derived from $\nu_{\rm peak}$. The uncertainty is $O(10^{-3})$.

(7) Line emission of [CII] 1900.543 GHz, [CII], CO(9-8) 1036.912 GHz and CO(4-3) 461.041 GHz, respectively.

(8) We estimate the $L_{\rm FIR}$ of ADF22-LineA, B and D by using the SED fitting method of Chary & Elbaz (2001). $L_{\rm FIR}$ of ADF22-LineC is referred to estimation of Umehata et al. (2017).

Funding

Acknowledgements

References

Asano, R. S., Takeuchi, T. T., Hirashita, H., & Nozawa, T. 2014, MNRAS, 440, 134

Aravena, M., Decarli, R., Walter, F., et al. 2016, ApJ, 833, 68

Aravena, M., Decarli, R., Walter, F., et al. 2016, ApJ, 833, 71

Barger, A. J., Wang, W.-H., Cowie, L. L., et al. 2012, ApJ, 761, 89

Behroozi, P. S., Wechsler, R. H., & Conroy, C. 2013, ApJ, 770, 57

Blain, A. W., Smail, I., Ivison, R. J., & Kneib, J.-P. 1999, MNRAS, 302, 632

Blain, A. W., Smail, I., Ivison, R. J., Kneib, J.-P., & Frayer, D. T. 2002, Phys. Rep., 369, 111

Bolzonella, M., Miralles, J.-M., & Pelló, R. 2000, A&A, 363, 476

Bouwens, R. J., Illingworth, G. D., Oesch, P. A., et al. 2012, ApJ, 754, 83

Bouwens, R. J., Aravena, M., Decarli, R., et al. 2016, ApJ, 833, 72

Brauher, J. R., Dale, D. A., & Helou, G. 2008, ApJS, 178, 280-301

Bruzual A., G., & Charlot, S. 1993, ApJ, 405, 538

Buat, V., Giovannoli, E., Burgarella, D., et al. 2010, MNRAS, 409, L1

Burgarella D., et al., 2013, A&A, 554, A70

Calzetti, D., Armus, L., Bohlin, R. C., et al. 2000, ApJ, 533, 682

Carniani, S., Maiolino, R., De Zotti, G., et al. 2015, A&A, 584, A78

Carniani, S., Maiolino, R., Pallottini, A., et al. 2017, arXiv:1701.03468

Casey, C. M., Narayanan, D., & Cooray, A. 2014, Phys. Rep., 541, 45

Capak, P. L., Carilli, C., Jones, G., et al. 2015, Nature, 522, 455

Carilli, C. L., & Walter, F. 2013, ARA&A, 51, 105

Chabrier, G. 2003, PASP, 115, 763

Chary, R., & Elbaz, D. 2001, ApJ, 556, 562

Chen, C.-C., Smail, I., Swinbank, A. M., et al. 2016, ApJ, 831, 91

Colbert J. W., et al., 1999, ApJ, 511, 721

Cox P., et al., 2011, ApJ, 740, 63

da Cunha, E., Walter, F., Decarli, R., et al. 2013, ApJ, 765, 9

Decarli, R., Walter, F., Carilli, C., et al. 2014, ApJ, 782, 78

Decarli, R., Walter, F., Aravena, M., et al. 2016, ApJ, 833, 69

Decarli, R., Walter, F., Aravena, M., et al. 2016, ApJ, 833, 70

De Looze I., Baes M., Bendo G. J., Cortese L., Fritz J., 2011, MNRAS, 416, 2712

De Looze, I., Cormier, D., Lebouteiller, V., et al. 2014, A&A, 568, A62

Díaz-Santos, T., Armus, L., Charmandaris, V., et al. 2013, ApJ, 774, 68

Díaz-Santos, T., Assef, R. J., Blain, A. W., et al. 2016, ApJL, 816, L6

Dunlop, J. S., McLure, R. J., Biggs, A. D., et al. 2017, MNRAS, 466, 861

Farrah, D., Lebouteiller, V., Spoon, H. W. W., et al. 2013, ApJ, 776, 38

Fujimoto, S., Ouchi, M., Ono, Y., et al. 2016, ApJS, 222, 1

Geach, J. E., & Papadopoulos, P. P. 2012, ApJ, 757, 156

Gehrels N., 1986, ApJ, 303, 336

Graciá-Carpio, J., Sturm, E., Hailey-Dunsheath, S., et al. 2011, ApJL, 728, L7

Gruppioni, C., Pozzi, F., Rodighiero, G., et al. 2013, MNRAS, 432, 23

Hainline, L. J., Blain, A. W., Smail, I., et al. 2009, ApJ, 699, 1610

Hatsukade, B., Kohno, K., Umehata, H., et al. 2016, PASJ, 68, 36

Hayashino, T., Matsuda, Y., Tamura, H., et al. 2004, AJ, 128, 2073

Herrera-Camus, R., Bolatto, A., Smith, J. D., et al. 2016, ApJ, 826, 175

Hemmati, S., Yan, L., Diaz-Santos, T., et al. 2017, ApJ, 834, 36

Hollenbach, D., & McKee, C. F. 1989, ApJ, 342, 306

Inoue, A. K. 2003, PASJ, 55, 901

Inoue, A. K., Shimizu, I., Tamura, Y., et al. 2014, ApJL, 780, L18

Inoue, A. K., Tamura, Y., Matsuo, H., et al. 2016, Science, 352, 1559

Iono, D., Yun, M. S., Elvis, M., et al. 2006, ApJL, 645, L97

Kapala, M. J., Sandstrom, K., Groves, B., et al. 2015, ApJ, 798, 24

Kaufman, M. J., Wolfire, M. G., Hollenbach, D. J., & Luhman, M. L. 1999, ApJ, 527, 795

Kennicutt, R. C., Jr. 1998, ApJ, 498, 541

Kousai, K, 2011, Ph.D. Thesis, Tohoku University.

Kroupa, P. 2001, MNRAS, 322, 231

Kubo, M., Uchimoto, Y. K., Yamada, T., et al. 2013, ApJ, 778, 170

Kubo, M., Yamada, T., Ichikawa, T., et al. 2015, ApJ, 799, 38

Lagos, C. d. P., Bayet, E., Baugh, C. M., et al. 2012, MNRAS, 426, 2142

Lehmer, B. D., Alexander, D. M., Geach, J. E., et al. 2009, ApJ, 691, 687

Madau, P., & Dickinson, M. 2014, ARA&A, 52, 415

Maiolino R., et al., 2005, A&A, 440, L51

Maiolino R., Caselli P., Nagao T., Walmsley M., De Breuck C., Meneghetti M., 2009, A&A, 500, L1

Maiolino R., et al., 2012, MNRAS, 425, L66

Maiolino R., Cox, P., Caselli, P., et al. 2005, A&A, 440, L51

Maiolino R., Carniani, S., Fontana, A., et al. 2015, MNRAS, 452, 54

Matsuda, Y., Yamada, T., Hayashino, T., et al. 2004, AJ, 128, 569

Matsuda, Y., Nagao, T., Iono, D., et al. 2015, MNRAS, 451, 1141

McMullin J. P., Waters B., Schiebel D., Young W., Golap K., 2007, ASPC, 376, 127

Miller, T. B., Chapman, S. C., Hayward, C. C., et al. 2016, arXiv:1611.08552

Nakamura, E., Inoue, A. K., Hayashino, T., et al. 2011, MNRAS, 412, 2579

Obreschkow, D., Croton, D., De Lucia, G., Khochfar, S., & Rawlings, S. 2009, ApJ, 698, 1467

Table 3. PHOTOMETRY.

ADF22 ID	u^*	B	V	R	i'	z'	J
ADF22-LineA,B	> 26.6	> 27.0	> 27.1	> 27.2	> 26.9	> 26.2	> 24.2
ADF22-LineD	23.84±0.05	23.46±0.03	22.86±0.01	22.08±0.01	21.47±0.01	21.13±0.01	19.79±0.01

ADF22 ID	H	K_s	3.6μm	4.5μm	5.8μm	8.0μm	24μm
ADF22-LineA,B	> 24.1	> 24.1	> 24.9	> 24.1	> 22.0	> 21.6	> 28.0
ADF22-LineD	20.21±0.02	19.39±0.01	19.49±0.01	19.88±0.02	19.81±0.05	20.04±0.10	16.46±0.10

NOTE. — All unit of photometry flux is AB magnitude. Upper limits are given by 3σ. The CFHT MegaCam u^* (in archive, P.I. Cowie, see also Matsuda et al. 2004). Subaru Suprime-Cam B, V, R, i', z' band (Matsuda et al. 2004), Subaru MOIRCS J, H, Ks (Uchimoto et al. 2012) and the Spitzer IRAC 3.6, 4.5, 5.8, 8.0 μm (Webb et al. 2009)-band photometry of the line emitters. The PSF difference in $u^* \sim 8.0$ μm are corrected following Kubo et al. (2013). The 24 μm photometry flux is calculated over a $2''$ diameter aperture.
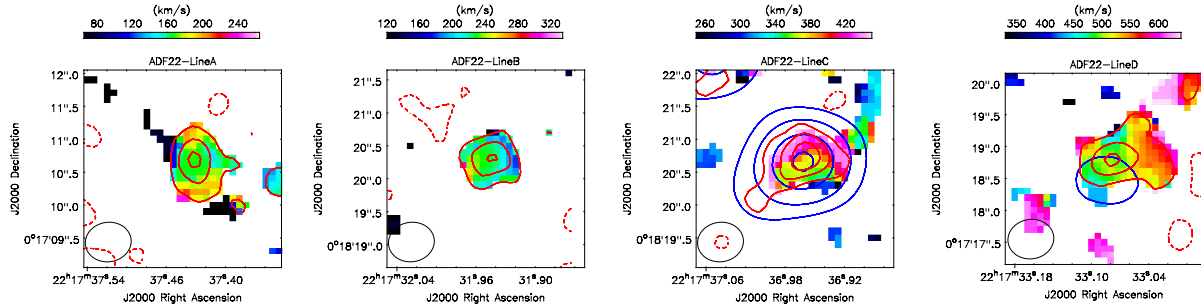

Fig. A. We plot the continuum-subtracted first moment maps of the four candidates. The images are made by using the spectrally smoothed data. The colormaps show the projected velocity field with $> 2\sigma$ around each target. The velocity is measured with respect to the center of each SPW. The red contours denote -2, 2, 4 and 6σ with negative contours shown by dashed line whereas the blue contours show the S/N ratio of continuum, with 4, 10, 20, 30σ. ADF22-LineA and LineB are not detected in 1.1 mm continuum. The beam size is shown at the bottom-left corner of each panel.
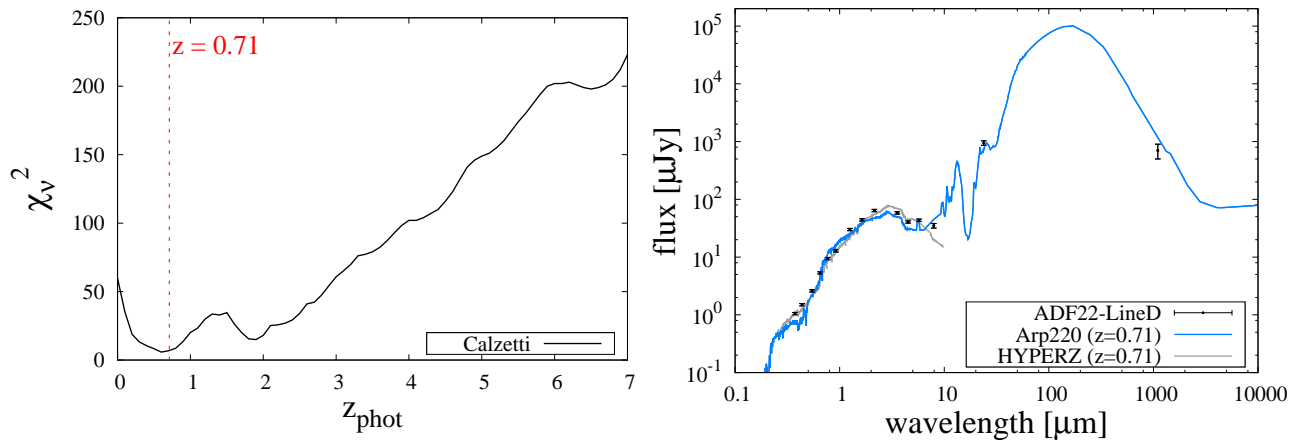

Fig. B. *Left* : The estimated reduced χ^2 as a function of photometric redshift for the ADF22-LineD (right). The χ_ν^2 value becomes minimum at $z = 0.6 - 0.8$. *Right* : The spectral energy distribution (SED) of ADF22-LineD (right). The SED is well fitted by that of Arp220 placed at $z \sim 0.71$.

Oesch, P. A., Bouwens, R. J., Illingworth, G. D., et al. 2014, ApJ, 786, 108

Omont, A., Yang, C., Cox, P., et al. 2013, A&A, 551, A115

Ono, Y., Ouchi, M., Kurono, Y., & Momose, R. 2014, ApJ, 795, 5

Orsi, Á., Padilla, N., Groves, B., et al. 2014, MNRAS, 443, 799

Pentericci, L., Carniani, S., Castellano, M., et al. 2016, ApJL, 829, L11

Polletta, M., Tajer, M., Maraschi, L., et al. 2007, ApJ, 663, 81

Popping, G., van Kampen, E., Decarli, R., et al. 2016, MNRAS, 461, 93

Rangwala, N., Maloney, P. R., Glenn, J., et al. 2011, ApJ, 743, 94

Salpeter, E. E. 1955, ApJ, 121, 161

Sargsyan L., et al., 2012, ApJ, 755, 171

Seaquist, E., Yao, L., Dunne, L., & Cameron, H. 2004, MNRAS, 349, 1428

Simpson, J. M., Swinbank, A. M., Smail, I., et al. 2014, ApJ, 788, 125

Smail I., Swinbank A. M., Ivison R. J., Ibar E., 2011, MNRAS, 414, L95

Smit, R., Bouwens, R. J., Franx, M., et al. 2012, ApJ, 756, 14

Speagle, J. S., Steinhardt, C. L., Capak, P. L., & Silverman, J. D. 2014, ApJS, 214, 15

Suzuki, R., Tokoku, C., Ichikawa, T., et al. 2008, PASJ, 60, 1347

Swinbank A. M., et al., 2012, MNRAS, 427, 1066

Swinbank, A. M., Simpson, J. M., Smail, I., et al. 2014, MNRAS, 438, 1267

Stacey, G. J., Hailey-Dunsheath, S., Ferkinhoff, C., et al. 2010, ApJ, 724, 957

Takeuchi, T. T., Hirashita, H., Ishii, T. T., Hunt, L. K., & Ferrara, A. 2003, MNRAS, 343, 839

Takeuchi, T. T., Buat, V., & Burgarella, D. 2005, A&A, 440, L17

Takeuchi, T. T., Ishii, T. T., Nozawa, T., Kozasa, T., & Hirashita, H. 2005, MNRAS, 362, 592

Tamura, Y., Saito, T., Tsuru, T. G., et al. 2014, ApJL, 781, L39

Uchimoto, Y. K., Yamada, T., Kajisawa, M., et al. 2012, ApJ, 750, 116

Umehata, H., Tamura, Y., Kohno, K., et al. 2015, ApJL, 815, L8

Umehata, H., Tamura, Y., Kohno, K., et al. 2017, ApJ, 835, 98

Vallini, L., Gruppioni, C., Pozzi, F., Vignali, C., & Zamorani, G. 2016, MNRAS, 456, L40

Venemans B. P., et al., 2012, ApJ, 751, L25

Wagg J., Carilli C. L., Wilner D. J., Cox P., De Breuck C., Menten K., Riechers D. A., Walter F., 2010, A&A, 519, L1

Wagg J., et al., 2012, ApJ, 752, L30

Webb, T. M. A., Yamada, T., Huang, J.-S., et al. 2009, ApJ, 692, 1561

Whiting, M. T. 2012, MNRAS, 421, 3242

Williams J. P., de Geus E. J., Blitz L., 1994, ApJ, 428, 693

Willott C. J., Omont A., Bergeron J., 2013, ApJ, 770, 13

Willott, C. J., Carilli, C. L., Wagg, J., & Wang, R. 2015, ApJ, 807, 180

Wolfire, M. G., Hollenbach, D., McKee, C. F., Tielens, A. G. G. M., & Bakes, E. L. O. 1995, ApJ, 443, 152

Wolfire, M. G., Hollenbach, D., & McKee, C. F. 2010, ApJ, 716, 1191

Vio, R., & Andreani, P. 2016, A&A, 589, A20

Yao, L., Seaquist, E. R., Kuno, N., & Dunne, L. 2003, ApJ, 588, 771

Zhao, Y., Lu, N., Xu, C. K., et al. 2016, ApJ, 819, 69

Zhou, L., Shi, Y., Diaz-Santos, T., et al. 2016, MNRAS, 458, 772